



This is a repository copy of *Estimation of valvular resistance of segmented aortic valves using computational fluid dynamics*.

White Rose Research Online URL for this paper:  
<http://eprints.whiterose.ac.uk/149359/>

Version: Accepted Version

---

**Article:**

Hoeijmakers, M.J.M.M., Soto, D.A.S., Wächter-Stehle, I. et al. (4 more authors) (2019) Estimation of valvular resistance of segmented aortic valves using computational fluid dynamics. *Journal of Biomechanics*. ISSN 0021-9290

<https://doi.org/10.1016/j.jbiomech.2019.07.010>

---

Article available under the terms of the CC-BY-NC-ND licence  
(<https://creativecommons.org/licenses/by-nc-nd/4.0/>).

**Reuse**

This article is distributed under the terms of the Creative Commons Attribution-NonCommercial-NoDerivs (CC BY-NC-ND) licence. This licence only allows you to download this work and share it with others as long as you credit the authors, but you can't change the article in any way or use it commercially. More information and the full terms of the licence here: <https://creativecommons.org/licenses/>

**Takedown**

If you consider content in White Rose Research Online to be in breach of UK law, please notify us by emailing [eprints@whiterose.ac.uk](mailto:eprints@whiterose.ac.uk) including the URL of the record and the reason for the withdrawal request.



[eprints@whiterose.ac.uk](mailto:eprints@whiterose.ac.uk)  
<https://eprints.whiterose.ac.uk/>

# Estimation of Valvular Resistance of Segmented Aortic Valves Using Computational Fluid Dynamics

M.J.M.M. Hoeijmakers<sup>a,b,\*</sup>, D.A. Silva Soto<sup>c</sup>, I. Wächter-Stehle<sup>d</sup>, M. Kasztelnik<sup>e</sup>, J. Weese<sup>d</sup>, D.R. Hose<sup>c</sup>, F.N. van de Vosse<sup>a</sup>

<sup>a</sup>*Cardiovascular Biomechanics Group, Department of Biomedical Engineering, Eindhoven University of Technology, PO Box 513 5600 MB, Eindhoven, The Netherlands*

<sup>b</sup>*ANSYS France, 69100 Villeurbanne, France*

<sup>c</sup>*Department of Infection, Immunity and Cardiovascular Disease, Medical Physics Group, University of Sheffield, Medical School, Beech Hill Road, S10 2RX, Sheffield, United Kingdom*

<sup>d</sup>*Philips Research Laboratories, Röntgenstrasse 24-26, D-22335, Hamburg, Germany*

<sup>e</sup>*Academic Computer Centre Cyfronet, AGH, University of Science and Technology, Kraków, Poland*

---

**\* ORIGINAL ARTICLE - REVISED VERSION.**

\*\*M.J.M.M. Hoeijmakers, Eindhoven University of Technology, De Rondom 70, Eindhoven, +31 (0)40 247 5675

\*Corresponding author

*Email address:* [m.j.m.m.hoeijmakers@tue.nl](mailto:m.j.m.m.hoeijmakers@tue.nl) (M.J.M.M. Hoeijmakers )

---

**Abstract**

Aortic valve stenosis is associated with an elevated left ventricular pressure and transaortic pressure drop. Clinicians routinely use Doppler ultrasound to quantify aortic valve stenosis severity by estimating this pressure drop from blood velocity. However, this method approximates the peak pressure drop, and is unable to quantify the partial pressure recovery distal to the valve. As pressure drops are flow dependent, it remains difficult to assess the true significance of a stenosis for low-flow low-gradient patients. Recent advances in segmentation techniques enable patient-specific Computational Fluid Dynamics (CFD) simulations of flow through the aortic valve. In this work a simulation framework is presented and used to analyze data of 18 patients. The ventricle and valve are reconstructed from 4D Computed Tomography imaging data. Ventricular motion is extracted from the medical images and used to model ventricular contraction and corresponding blood flow through the valve. Simplifications of the framework are assessed by introducing two simplified CFD models: a truncated time-dependent and a steady-state model. Model simplifications are justified for cases where the simulated pressure drop is above 10 mmHg. Furthermore, we propose a valve resistance index to quantify stenosis severity from simulation results. This index is compared to established metrics for clinical decision making, i.e. blood velocity and valve area. It is found that velocity measurements alone do not adequately reflect stenosis severity. This work demonstrates that combining 4D imaging data and CFD has the potential to provide a physiologically relevant diagnostic metric to quantify aortic valve stenosis severity.

*Keywords:* Aortic valve stenosis, Heart valve disease, Hemodynamics, Computational fluid dynamics, Patient-specific

---

## 1. Introduction

Aortic valve stenosis (AS) is the narrowing of the aortic valve ~~at the location of the aortic valve~~ and ~~disturbs impedes~~ blood flow into the systemic circulation. Once developed, AS consistently increases with age, and it is [1] R 1.5. estimated that 2.8-3.9% of the population older than 70 years of age suffer from some form of AS (Eveborn et al., 2012; Nkomo et al., 2006). AS is often caused by calcification of the Aortic Valve (AV) leaflets, resulting in a stiffer valve that impedes the opening and closing function of the valve. Hence, in systole, the valve may not open completely, and a large pressure difference is required to maintain flow. If left untreated, AS may eventually lead to heart failure.

AS obstructs flow from the ventricle into the aorta, and a large effective pressure difference is required to maintain cardiac output. The drop in pressure is an indicator for the severity of AS. However, non-invasive diagnostic quantitative evaluation of the pressure drop is challenging. Hence, in current clinical practice other indirect metrics are used. At present, the main criteria to judge AS severity are: the mean transaortic pressure drop; maximum velocity of the jet ( $v_{\max}$ ), and the Aortic Valve Area (AVA) by continuity equation (Chambers, 2016; Nishimura et al., 2014; Baumgartner et al., 2016). All these metrics are routinely obtained by echocardiography. However,  $v_{\max}$  and the mean pressure drop are both flow-dependent, and may conflict with AVA measurements for 20-30% of patients with severe AS (Eleid et al., 2013). ~~Typically, these diagnostic measures conflict for cases with low-flow/low-gradient AS.~~ For this patient group it remains difficult to assess whether AS is significantly present (Vogelgesang et al., 2017).

Echocardiography is inexpensive, readily available and easy to perform, and an established method to derive metrics indicative of stenosis severity. When echocardiography results are inconclusive, Computed Tomography (CT) or cardiac Magnetic Resonance Imaging (MRI) can be used to derive additional indicators, e.g the aortic diameter or amount of calcification (Chun et al., 2008). Furthermore, CT and cardiac MRI enable detailed three-dimensional recon-

31 structions of the full-heart anatomy. Moreover, segmentation methods from  
 32 cardiac CT and MRI images have improved considerably over the past years  
 33 (Ecabert et al., 2008, 2011; Grbic et al., 2012; Ionasec et al., 2010). Further-  
 34 more, recent developments see high-quality valve models incorporated into ex-  
 35 isting segmentation frameworks (Weese et al., 2017). These detailed 3D models  
 36 of the AV can be used in combination with 3D Computational Fluid Dynamics  
 37 (CFD) to evaluate the hemodynamic performance of the patient-specific valve  
 38 (Weese et al., 2017). However, in order to quantify the load on the ventricle,  
 39 extending the CFD model to include the (contracting) Left Ventricle (LV) may  
 40 yield information on the true significance of the stenotic valve.

41 In systole, a healthy valve opens completely, and imposes little to no re-  
 42 sistance to blood flow. However, flow through the diseased valve is similar to  
 43 flow through an orifice. Blood is accelerated into the orifice, and pressure is  
 44 converted to kinetic energy. When blood enters the Ascending Aorta (AA), it  
 45 is decelerated, and pressure is partly recovered. (Fig. 1). Pressure is not com-  
 46 pletely recovered due to viscous losses, including those from turbulence. This  
 47 results in an effective pressure drop between the LV and AA. To quantify the  
 48 relative contribution of the valve to the effective pressure drop, a valve resistance  
 49 index is proposed:

$$I_{VR} = \frac{\Delta P_V}{\Delta P_E} \quad (1)$$

50 This index quantifies the pressure loss due to the presence of the valve ( $\Delta P_V$ )  
 51 with respect to the total effective pressure loss between the LV and AA ( $\Delta P_E$ ).  
 52 For healthy valves, pressure is expected to recover approximately to the same  
 53 pressure level as in the Left Ventricular Outflow Tract (LVOT). **When the cross-**  
 54 **sectional area of the AA exceeds that of the LVOT, blood velocity (and kinetic**  
 55 **energy) in the AA decrease. Consequently, (static) pressure may recover be-**  
 56 **yond LVOT pressure.** However, for diseased valves, it is expected that only a  
 57 (small) part of pressure is recovered, and excessive viscous and turbulent losses  
 58 dominate.

[2] R 1.7.

59 The main aim of this work is to evaluate the valve resistance index pro-  
60 posed in Equation 1 with clinically accepted measures, such as,  $v_{\max}$  and the  
61 AVA. Additionally, the CFD model with the contracting left ventricle is used  
62 to evaluate the accuracy of simplified valve-only CFD models and Bernoulli ap-  
63 proximations. For this purpose, the workflow described by Weese *et al.* (Weese  
64 *et al.*, 2017) is extended to include both the AV and contracting ventricle.

## 65 2. Materials and Methods

### 66 2.1. Aortic Valve Anatomies

67 Cardiac CT segmentation data was obtained from an anonymized dataset  
68 used in a previous study (Weese *et al.*, 2017). Original images were acquired  
69 using electrocardiogram-gated CT angiography with 10% intervals of the elec-  
70 trocardiographic R-R interval. CT images had an in-plane resolution of 0.31-  
71 0.68 mm and slice thickness of 0.34-0.70 mm. Segmented anatomical structures  
72 include the LV, LVOT and AV. Fig. 2B shows a typical segmented anatomy at  
73 different phases of the cardiac cycle.

74 A single Structured Surface models of the LV and AV throughout systole was  
75 were generated for each patient with a Shape Constrained Deformable Model  
76 (SCDM). The authors refer to Ecabert *et al.* or Weese *et al.* for a detailed  
77 description of the SCDM (Ecabert *et al.*, 2008, 2011; Weese *et al.*, 2017). The  
78 surface model was built from the image at mid-systole was selected, and de-  
79 veloped into the CFD model. This model had the valve in the most open  
80 position, typically at 20% or 30% of the electrocardiographic R-R interval. The  
81 structured surface model consisted of 3094 vertices and 6169 triangles with an  
82 average edge length of 2.6 mm (Fig. 2B). The geometric AVA was estimated  
83 from the structured surface model by a projection method (Weese *et al.*, 2017).  
84 All segmentation surface models throughout the cardiac cycle were then con-  
85 verted into binary masks, covering the LV and LVOT, to facilitate registration.

86 

---

 [3] R 1.6.

87 *2.2. Image Registration*

88 Each consecutive ~~segmented~~ binarized image pair was registered using The  
89 Sheffield Image Registration Toolkit (Barber & Hose, 2005). The resulting 3D  
90 discrete mapping fields morphed one image onto the next. The Sheffield Image  
91 Registration Toolkit produced smooth, non-linear registration maps with sub-  
92 pixel accuracy. To compute the 3D mappings between the images, the Sheffield  
93 Image Registration Toolkit uses an intensity-based linear least-squares algo-  
94 rithm, iteratively applied to handle large displacements. The 3D registration  
95 map was spatially interpolated to the vertices of the surface model at mid-  
96 ~~systole. This yielded a set of iso-topological surface models in the R-R interval~~  
97 ~~This yielded a set of surface models in the R-R interval with the same topology~~  
98 ~~as the surface model at mid-systole.~~ Registration was done on the binarized  
99 ~~segmented~~ images, hence no information on the motion of the AV and AA was  
100 available. For this reason, and for CFD stability the mean rigid motion of the  
101 model was removed from the overall model motion. Velocity vectors  $\vec{v}$  for each  
102 vertex  $n$  of the surface model were a function of time and computed from the  
103 consecutive iso-topological surface models by:

$$\vec{v}_n(t) = \frac{\vec{x}_n(t + \Delta t) - \vec{x}_n(t)}{\Delta t} \quad (2)$$

104 With  $\vec{x}$  the position of vertex  $n$  at time  $t$  in the cardiac cycle. Vertex positions  
105 are sparse in time, and were interpolated using cubic splines.

106 *2.3. Mesh Generation*

107 Volumetric meshing was performed with ANSYS Fluent Meshing R17.2 (AN-  
108 SYS Inc, Canonsburg, Pennsylvania, United States). Structured surface models  
109 were truncated by a ~~manually defined~~ plane ~~two to~~ five mm proximal to the valve  
110 ~~annulus~~base and orthogonal to the valve axis (Fig. 2C). The outflow boundary  
111 was extended by 3.5 times the diameter of the AA. The inflow boundaries of the  
112 truncated models were extended by 1.5 times the LVOT diameter. The volume  
113 was filled with tetrahedra in the core, and ten layers of pentahedra elements

114 inflated from the wall. Element sizes were chosen based on a mesh sensitivity  
 115 study, and ranged between 0.5-2.5 mm. Maximum element edge length in the  
 116 LV was constrained to 2.5 mm. Edge lengths in the proximity of the AV were  
 117 constrained to 0.5 mm to capture valve features.

#### 118 2.4. Computational Methods

119 Fluid flow is governed by the Navier-Stokes equations. For moving grids,  
 120 the integral form of the continuity equation for a control volume  $\Omega$  with surface  
 121  $\Gamma$  can be written as.

$$\frac{\partial}{\partial t} \int_{\Omega} \rho dV + \int_{\Gamma} \rho(\vec{v} - \vec{v}_g) \cdot \vec{n} dA = 0 \quad (3)$$

122 With  $\rho$  the density of blood,  $\vec{v}$  the velocity vector,  $\vec{v}_g$  the velocity of the (bound-  
 123 ary) grid, and  $\vec{n}$  the normal vector to the surface  $\Gamma$ . Similarly, the momentum  
 124 equation can be written as:

$$\frac{\partial}{\partial t} \int_{\Omega} (\rho \vec{v}) dV + \int_{\Gamma} \rho \vec{v}(\vec{v} - \vec{v}_g) \cdot \vec{n} dA = - \int_{\Gamma} p \mathbf{I} \cdot \vec{n} dA + \int_{\Gamma} \boldsymbol{\tau} \cdot \vec{n} dA \quad (4)$$

125 Where  $p$  is the pressure,  $\mathbf{I}$  the identity tensor, and  $\boldsymbol{\tau}$  the viscous stress tensor.  
 126 A diffusion based smoothing method was applied for grid motion.

$$\nabla \cdot (\gamma \nabla \vec{v}_g) = 0 \quad (5)$$

$$\gamma = \frac{1}{d^\alpha} \quad (6)$$

127 With  $\vec{v}_g$  the grid velocity,  $\gamma$  the diffusion coefficient and  $d$  the normalized dis-  
 128 tance to the boundary. For all simulations  $\alpha = 1$  and resulted in skewed grid  
 129 motion towards the interior, i.e. elements in the interior deformed more. The  
 130 boundary conditions (Fig. 3) for the diffusion equation were:



$$\begin{aligned}\Gamma_{AA}, \Gamma_{Sinus}, \Gamma_{AV} : \vec{v}_g &= 0 \\ \Gamma_{LVOT} : \vec{v}_g &= f(s)\vec{v}_n(t) \\ \Gamma_{LV} : \vec{v}_g &= \vec{v}_n(t)\end{aligned}$$

131  $f(s)$  is a ramp function that linearly scaled boundary velocity to zero in the  
 132 LVOT as a function of the position  $s$  in the LVOT, i.e.  $f(s) = 1$  proximal to  
 133 the LVOT, and  $f(s) = 0$  distal to the LVOT.

134 Blood was modeled as an in-compressible fluid with a density of  $1050 \text{ kg}\cdot\text{m}^{-3}$   
 135 and dynamic viscosity of  $0.004 \text{ Pa}\cdot\text{s}$ . No-slip boundary conditions were as-  
 136 sumed at the walls, and at boundary  $\Gamma_{out}$  pressure is set to zero. The governing  
 137 equations were solved with ANSYS Fluent R17.2 (ANSYS Inc, Canonsburg,  
 138 Pennsylvania, United States). Simulations were executed on the ACC Cyfronet  
 139 AGH Prometheus Supercomputer (Academic Computer Centre Cyfronet, AGH  
 140 University of Science and Technology, Kraków, Poland). Each simulation was  
 141 assigned one compute node with 24 CPU's.

#### 142 2.4.1. Transient Models

143 For the transient models a (bounded) central difference scheme was used for  
 144 the advection and diffusion terms. The transient term was integrated with a  
 145 second order backward difference approximation. Convergence criteria at each  
 146 time-step were set at 0.05 for locally scaled residuals of x-, y-, z-velocity, and  
 147 continuity. Sub-grid turbulent dissipation was modeled with Large Eddy Sim-  
 148 ulation and the Wall Adapting Local Eddy-Viscosity model (Nicoud & Ducros,  
 149 1999). Time steps were defined as 1/10000th of the cardiac cycle. Vertex ve-  
 150 locities were spatially interpolated from the structured surface model onto the  
 151 re-meshed surface of the computational domain by an inverse distance-weighted  
 152 interpolation using eight nearest neighbors of the structured model. Stroke vol-  
 153 ume was pre-computed with a discrete form of Gauss's theorem (Hughes et al.,  
 154 1996) for the structured and re-meshed surfaces. Vertex velocities of the refined  
 155 computational mesh were scaled to match the stroke volume of the structured

156 surface model. The time-dependent grid velocity was applied to the boundary  
157 of the LV and LVOT. For the truncated model, the pre-computed flow wave-  
158 form was used as a time-dependent plug-flow boundary condition. [To test](#)  
159 [whether diastolic filling of the ventricle had to be simulated, five cardiac cycles](#)  
160 [were simulated for case 11. Results in Table 1 demonstrate that diastolic filling](#)  
161 [had a negligible \(< 1%\) effect on the observed peak-systolic pressure drop and](#)  
162 [valve resistance index. Hence, diastolic filling was neglected, and only a single](#)  
163 [systolic cycle was simulated to restrict the computational burden.](#)

[4] R 1.1 &  
1.2

#### 164 2.4.2. Steady-state Model

165 Peak flow-rate was obtained from the pre-computed flow waveform, and  
166 prescribed as a boundary condition for the truncated steady-state model. Tur-  
167 bulence is modeled with the Shear Stress Transport  $k-\omega$  model (Menter, 1994).

#### 168 2.5. Post-Processing

169 A centreline with equally spaced points (0.1mm intervals) was defined for  
170 each surface model with the Vascular Modelling Toolkit (Antiga et al., 2008).  
171 Pressure was evaluated on the centreline, and the effective ( $\Delta P_E$ ) and valve  
172 ( $\Delta P_V$ ) pressure-drops were computed. These pressure drops were used to com-  
173 pute the valve resistance index  $I_{VR}$  (Equation 1). Furthermore, Bernoulli esti-  
174 mates ( $\Delta P_B = P_{LVOT} - P_{VC}$ ) and simplified Bernoulli estimates ( $\Delta P_{SB} = 4v_{VC}^2$ )  
175 were computed from the simulation results. Note that  $v_{VC}$  is the velocity at the  
176 vena contracta, and corresponds to  $v_{max}$ . The point on the centreline closest  
177 to the truncation plane was used to evaluate  $P_{LVOT}$ . The vena contracta was  
178 identified by inspecting the centreline, i.e. where pressure was lowest.

[5] Note  
that a  
slightly  
larger  
timestep  
and coarser  
mesh was  
used to facil-  
itate reason-  
able simu-  
lation times  
- hence re-  
sults differ  
slightly from  
the original  
simulations

### 179 3. Results

180 The workflow described in Fig. 2 was used on retrospective CT datasets of  
181 18 patients with non-calcified and (partially) severely calcified tricuspid AV's  
182 (Fig. 4). Projected AVA ranged between 0.90-88 and 4.34-35 cm<sup>2</sup> (Table 2).  
183 Image derived maximum flow rate at peak systole ranged between 178 and 635

184 ml/s, and simulated velocities in the vena contracta range between 0.88 and  
185 5.36 m/s. The effective pressure drop  $\Delta P_E^{CLV}$  ranges between 2.5 and 102.5  
186 mmHg. Net pressure drops across the aortic valve range between: -2.3 mmHg  
187 and 91.5 mmHg for the full model; -1.4 mmHg and 89.5 mmHg for the truncated  
188 transient model; 0.4 mmHg and 89.8 mmHg for the steady-state model.  $\Delta P_B^{CLV}$   
189 and  $\Delta P_{SB}^{CLV}$  range between 1.0-103.2 mmHg and 3.1-115.1 mmHg. The valve  
190 resistance index lies between -0.40 and 0.96. [The local pressure gradient in the](#)  
191 [LVOT was between -0.77 and -0.07 mmHg/mm](#)

192 Fig. 5 illustrates the CFD results of a healthy (case 8) and a stenotic valve  
193 (case 17). The healthy case exhibits a lower jet velocity through the AV than  
194 the stenotic case. For the stenotic valve a distinct jet is formed, and turbulent  
195 structures develop. The jet is wider and not as pronounced for the healthy valve.  
196 Pressure contours demonstrate that the the effective pressure drop between  
197 the LV and AA is about 9 mmHg for the healthy case [and approximately 110](#)  
198 [mmHg for the stenotic case. in the healthy case. The effective pressure drop is](#)  
199 [substantially larger \(approximately 110 mmHg\) for the stenotic valve.](#)

200 Fig. 6 visualizes the relationship between  $v_{max}$  and the proposed valve resis-  
201 tance index. When assessing AS severity by  $v_{max}$ , 12 cases would be considered  
202 healthy, one case as having a mild stenosis, and three as having a moderate  
203 stenosis. Two cases would be classified as having a severe stenosis. Cases 15  
204 and 16 would be classified as having no or a mild stenosis. However, both exhibit  
205 large valve resistance indices of 0.84 and 0.86 respectively, of similar magnitude  
206 as the clearly stenotic cases 13 and 17. Furthermore, it is observed that case 18,  
207 actually has the largest valve resistance index, but would have been classified as  
208 moderate with  $v_{max}$  as criteria. Healthy valves exhibit valve resistance indices  
209 close to or below zero. Furthermore, an inverse linear relationship between geo-  
210 metric AVA and valve resistance index may be observed; when AVA decreases,  
211 the valve resistance index increases. (Fig. 6).

212 Fig. 7A and 7B qualitatively demonstrate the differences between each of  
213 the CFD models. Unsteady flow phenomena distal to the AV are observed.  
214 Flow patterns for the transient models are similar, but local discrepancies in

215 the velocity field can be noticed. Unsteady flow patterns propagate far into the  
216 AA for this particular stenotic case.

217 Qualitatively the shape of the jet and the pressure contours are similar prox-  
218 imal to and in the immediate vicinity of the valve for the steady-state and  
219 transient models (Fig. 7). However, flow structures distal to the valve are less  
220 well-matched. This is expected because the jet has not had time to develop fully  
221 in space for the transient models. Despite the loss of fidelity in the detailed flow  
222 fields, the steady-state model captures the overall pressure drop adequately.  
223 Pressures proximal to the AV, in the vena contracta and distal to the AV are  
224 approximately the same for all models.

225 Differences in  $\Delta P_V$  of  $0.3 \pm 1.33$  and  $0.9 \pm 1.63$  are found between the tran-  
226 sients models, and truncated steady and full model respectively (Fig. 8A and  
227 B). A bias of  $0.7 \pm 1.07$  mmHg is observed between both truncated models (Fig.  
228 8C). The simplified Bernoulli and full 4D CFD model are in poor agreement: a  
229 bias of  $11.3 \pm 6.6$  mmHg (Fig. 9B). At low flow the simplified Bernoulli equation  
230 gives a poor estimate for the peak-systolic effective pressure-drop. Bernoulli  
231 estimates demonstrate a bias of  $6.6 \pm 3.27$  mmHg compared to the full model. In  
232 general, discrepancies from the full model predominantly occur at low pressure  
233 pressure drops (Fig 8 and 9). E.g., the relative difference between  $\Delta P_V^{CLV}$  and  
234  $\Delta P_V^{TT}$  for case 6 is 140%. In contrast, a relative difference of only 2% is found  
235 for case 17.

#### 236 4. Discussion

237 This paper presents a medical image-based CFD framework to simulate flow  
238 across a patient-specific AV. A valve resistance index is defined, and compared  
239 to measures typically used in the clinic [to demonstrate the frameworks poten-](#)  
240 [tial value](#). Additionally, the effect of model simplifications on pressure-drop  
241 computations are presented.

242 *4.1. Sample characteristics*

243 Computed geometric AVA's (Table 2) suggest that the current sample con-  
244 tains 11 healthy or mildly stenosed cases, six moderate cases, and one severe  
245 case (Nishimura et al., 2014). When considering  $v_{\max}$  as severity index, it is  
246 found that 12 cases can be classified as healthy, one as mild, three as moderate,  
247 and two as having a severely stenotic valve. Unfortunately, no echocardiography  
248 or cardiac catheterization data was available to clinically classify the patients.  
249 Nevertheless, computed velocities, pressure-drops and AVA correspond well to  
250 values reported in literature (Chambers, 2016; Baumgartner et al., 1999). For  
251 example, cardiac catheterization and echocardiography measurements in AS pa-  
252 tients by Yang *et al* show systolic pressure drops between the LV and AA up  
253 to 129 mmHg for patients with (echocardiography derived) AVA's of 0.4 cm<sup>2</sup>  
254 (Yang et al., 2015). Furthermore, the same study reports echocardiography  
255 based peak-systolic  $v_{\max}$  measurements of 2.3 - 5.2 m/s. The reported upper  
256 limits for  $\Delta P_E$  and  $v_{\max}$  in this study are 103 mmHg and 5.4 m/s, and thus  
257 respect the limits typically reported in literature.

258 *4.2. Valve Resistance Index*

259 The valve resistance index is a measure of how much pressure is lost due to  
260 the presence of the AV. This index can be interpreted as a percentage, e.g. an  
261 index of 0.60 means that 60% of pressure loss can be attributed to the AV. Figure  
262 6 demonstrates that healthy valves (cases 1-9) have valve resistance indices of  
263 around zero, i.e. any pressure lost around the AV is fully recovered in the AA.  
264 For some cases, recovered pressure even exceeds pressure in the LVOT (cases  
265 1-3). This can be explained by the fact that the cross-sectional area of the  
266 AA is typically two to three times larger than the cross-sectional area of the  
267 LVOT (see Table 2). Due to the larger cross-sectional area, velocity in the AA  
268 will be lower, and more kinetic energy is converted back into static pressure.  
269 Hence, pressure may recover beyond that of the LVOT, leading to a negative  
270 valve resistance index. Therefore, a healthy valve, in its open position, exerts  
271 no additional load on the left ventricle at peak systole. For severely stenotic

[6] R 1.7.

272 valves, the valve dominates the effective pressure drop (cases 17 and 18), i.e.  
273 approximately 90% of the effective pressure drop is attributed to the AV. This is  
274 in line with numerical results presented by Traeger *et al* (Traeger et al., 2015).  
275 Although not the main aim of their work, their illustrations suggest that a valve  
276 with an area of 0.9 cm<sup>2</sup> (Gorlin derived) may exhibit a valve resistance index  
277 of approximately 0.9 at flow rates of 200 and 400 ml/s.

278 Figure 6 clearly demonstrates the inability of  $v_{\max}$  to identify a stenosis  
279 consistently. Due to low-flow, cases 15 and 16 demonstrate a  $v_{\max}$  that would  
280 be considered normal, or mildly stenotic in clinical practice. However, the valve  
281 resistance index for these cases reveals that - similar to other stenotic valves -  
282 the effective pressure drop is dominated by the AV. A disproportional amount  
283 of the pressure loss is due to the presence of the valve. Such a conclusion can  
284 not be drawn from  $v_{\max}$  (Fig. 6) and  $\Delta P_E$  measurements alone. Hence, for  
285 cases where AVA and  $v_{\max}$  conflict, ~~indistinct cases~~ the valve resistance index  
286 may provide relevant information on stenosis severity.

#### 287 4.3. Comparison CFD Models

288 Qualitatively, no major differences are observed between the transient mod-  
289 els (Fig. 7). Similar (turbulent) structures are formed distal to the AV where  
290 the jet breaks down, and pressure is recovered. Steady-state simulations demon-  
291 strate averaged velocity and pressure distributions, and do not capture local flow  
292 disturbances in detail. Nevertheless, steady-state simulations capture the global  
293 pressure drop across the AV within reasonable limits. Both truncated models  
294 provide acceptable estimates for the pressure drop across the AV. At low pres-  
295 sure drops (<10 mmHg) the truncated models overestimate the pressure drop  
296 considerably in the relative sense. An artificial plug-flow assumption at the  
297 inflow boundary may not be appropriate for the low-gradient cases. Indeed,  
298 velocity profiles in the LVOT are not plug-like (Garcia et al., 2011). Work  
299 by Bruening and colleagues shows that significant overestimation of the pres-  
300 sure drop can occur when assuming a plug-flow velocity profile opposed to a  
301 patient-specific flow profile from 4D velocity-encoded MRI (Bruening et al.,

302 2018). However, differences between the full and truncated transient model are  
303 small in this study, and the added accuracy of the full model may therefore not  
304 outweigh the additional computational cost.

305 The simplified Bernoulli equation - derived from echocardiography measure-  
306 ments in the clinic - overestimates the pressure drop substantially. Overestima-  
307 tion of the pressure drop is a well known problem with the Simplified Bernoulli  
308 equation. Both numerical (Casas et al., 2015; Donati et al., 2017) and pa-  
309 tient studies (Baumgartner et al., 1999) have demonstrated this overestimation.  
310 It should be noted that  $v_{\max}$  is directly obtained from the simulated velocity  
311 field. Clinically, measurements are done with echocardiography, and additional  
312 sources of errors are likely, such as: poor spatial resolution, misalignment of the  
313 probe, or probe settings (Lui et al., 2005).

#### 314 4.4. Limitations Imaging and Geometry

315 Segmentation with the SCDM is at the moment only possible for tri-cuspid  
316 AV's. Substantial segmentation errors are expected for bicuspid valves. Weese  
317 et al (Weese et al., 2017) showed that segmentation works in presence of calci-  
318 fications. However, strong calcifications are likely to influence segmentation ac-  
319 curacy and blood flow. Hence, a thorough evaluation of segmentation accuracy  
320 is required. For example, it may be necessary to map patient-specific calcifica-  
321 tions onto the shape constrained deformable model. Further inaccuracies may  
322 be introduced by the registration process.

[7] R 1.4.

323 Segmentation is performed on electrocardiography triggered CT images at  
324 10% intervals of the R-R curve. It is assumed that the temporal resolution is  
325 sufficient to capture the (fully) open state of the AV. Poor temporal resolution  
326 may also cause over- or underestimation of flow-rate. Mitral regurgitation is  
327 not quantified, and patient flow-rates are likely overestimated. For example,  
328 patients with severe Mitral valve regurgitation may see a regurgitant fraction of  
329 more than 50% (Zoghbi et al., 2017).

#### 330 4.5. Limitations CFD

331 No valvular fluid-solid interaction is considered in this study due to the nu-  
332 merical challenges and lack of patient-specific material properties. It is expected  
333 that only local intraventricular and aortic flow fields are influenced. It is not  
334 expected that peak-systolic pressure drops and  $v_{\max}$  are affected. Work by As-  
335 torino *et al.* supports this choice. Their work suggests that modeling the valve  
336 in the fixed open position yields an acceptable approximation for flow at peak  
337 systole, opposed to simulating the fully coupled fluid-solid interaction (Astorino  
338 *et al.*, 2012).

339 The multi-cycle simulations that were performed on case 11 lacked the  
340 patient-specific mitral valve. As such, end-diastolic flow patterns may not be  
341 physiologically correct. For example, a recent study showed that mitral valve  
342 opening dynamics and shape substantially influence end-diastolic vortex forma-  
343 tion (Vasudevan *et al.*, 2019). Whether the single-cycle approach is still accept-  
344 able in the presence of the segmented mitral valve has not been investigated.

345

## 346 5. Conclusion

347 An image-based CFD workflow of the AV and heart anatomy is presented.  
348 This workflow allows for the computation of a valve resistance index, that quan-  
349 tifies the contribution of the AV to the effective pressure drop from the LV to  
350 the AA. It is demonstrated that this index ~~has the potential to complement~~  
351 ~~the potential to outperform~~ existing measures, such as,  $v_{\max}$  and the geomet-  
352 ric AVA ~~for patients that demonstrate discordant grading~~. Furthermore, it is  
353 shown that simplified CFD models provide a reasonable estimate of the aortic  
354 valve pressure drop at a given flow rate. However, at low-flow conditions simpli-  
355 fications to boundary conditions may not be justified, and more physiologically  
356 accurate inflow boundary conditions should be considered.



357 **Acknowledgements**

358 This work was supported in part by the European Research Council Grant  
359 (Grant number: 689617) and by the PLGrid Infrastructure. The authors would  
360 like to thank V. Morgenthaler for his valuable technical input.

361 **Conflicts of Interest**

362 M.J.M.M. Hoeijmakers is an employee of ANSYS. J. Weese and I. Wächter-  
363 Stehle are employees of Philips.

364 **References**

- 365 Antiga, L., Piccinelli, M., Botti, L., Ene-Iordache, B., Remuzzi, A., & Steinman,  
366 D. A. (2008). An image-based modeling framework for patient-specific com-  
367 putational hemodynamics. *Medical & Biological Engineering & Computing*,  
368 *46*, 1097–1112. doi:[10.1007/s11517-008-0420-1](https://doi.org/10.1007/s11517-008-0420-1).
- 369 Astorino, M., Hamers, J., Shadden, S. C., & Gerbeau, J.-F. (2012). A ro-  
370 bust and efficient valve model based on resistive immersed surfaces. *Interna-  
371 tional Journal for Numerical Methods in Biomedical Engineering*, *28*, 937–  
372 959. doi:[10.1002/cnm.2474](https://doi.org/10.1002/cnm.2474).
- 373 Barber, D., & Hose, D. (2005). Automatic segmentation of medical images using  
374 image registration: diagnostic and simulation applications. *Journal of Medical  
375 Engineering & Technology*, *29*, 53–63. doi:[10.1080/03091900412331289889](https://doi.org/10.1080/03091900412331289889).
- 376 Baumgartner, H., Hung, J., Bermejo, J., Chambers, J. B., Edvardsen, T., Gold-  
377 stein, S., Lancellotti, P., LeFevre, M., Miller, F., & Otto, C. M. (2016). Rec-  
378 ommendations on the echocardiographic assessment of aortic valve stenosis: a  
379 focused update from the european association of cardiovascular imaging and  
380 the american society of echocardiography. *European Heart Journal - Cardio-  
381 vascular Imaging*, *18*, 254–275. doi:[10.1093/ehjci/jew335](https://doi.org/10.1093/ehjci/jew335).

- 382 Baumgartner, H., Stefenelli, T., Niederberger, J., Schima, H., & Maurer, G.  
383 (1999). "overestimation" of catheter gradients by doppler ultrasound in pa-  
384 tients with aortic stenosis: a predictable manifestation of pressure recovery.  
385 *Journal of the American College of Cardiology*, *33*, 1655–1661.
- 386 Bruening, J., Hellmeier, F., Yevtushenko, P., Kelm, M., Nordmeyer, S.,  
387 Sündermann, S. H., Kuehne, T., & Goubergrits, L. (2018). Impact of  
388 patient-specific LVOT inflow profiles on aortic valve prosthesis and ascend-  
389 ing aorta hemodynamics. *Journal of Computational Science*, *24*, 91–100.  
390 doi:[10.1016/j.jocs.2017.11.005](https://doi.org/10.1016/j.jocs.2017.11.005).
- 391 Casas, B., Lantz, J., Dyverfeldt, P., & Ebbers, T. (2015). 4d flow MRI-based  
392 pressure loss estimation in stenotic flows: Evaluation using numerical simu-  
393 lations. *Magnetic Resonance in Medicine*, *75*, 1808–1821. doi:[10.1002/mrm.](https://doi.org/10.1002/mrm.25772)  
394 [25772](https://doi.org/10.1002/mrm.25772).
- 395 Chambers, J. B. (2016). The assessment of aortic stenosis: echocardiography  
396 and beyond. *British journal of hospital medicine (London, England : 2005)*,  
397 *77*, 141–146. doi:[10.12968/hmed.2016.77.3.141](https://doi.org/10.12968/hmed.2016.77.3.141).
- 398 Chun, E. J., Choi, S. I., Lim, C., Park, K.-H., Chang, H.-J., Choi, D.-J., Kim,  
399 D. H., Lee, W., & Park, J. H. (2008). Aortic stenosis: Evaluation with mul-  
400 tidetector CT angiography and MR imaging. *Korean Journal of Radiology*,  
401 *9*, 439. doi:[10.3348/kjr.2008.9.5.439](https://doi.org/10.3348/kjr.2008.9.5.439).
- 402 Donati, F., Myerson, S., Bissell, M. M., Smith, N. P., Neubauer, S., Monaghan,  
403 M. J., Nordsletten, D. A., & Lamata, P. (2017). Beyond BernoulliCLINICAL  
404 PERSPECTIVE. *Circulation: Cardiovascular Imaging*, *10*, e005207. doi:[10.](https://doi.org/10.1161/circimaging.116.005207)  
405 [1161/circimaging.116.005207](https://doi.org/10.1161/circimaging.116.005207).
- 406 Ecabert, O., Peters, J., Schramm, H., Lorenz, C., von Berg, J., Walker, M.,  
407 Vembar, M., Olszewski, M., Subramanyan, K., Lavi, G., & Weese, J. (2008).  
408 Automatic model-based segmentation of the heart in CT images. *IEEE Trans-*  
409 *actions on Medical Imaging*, *27*, 1189–1201. doi:[10.1109/tmi.2008.918330](https://doi.org/10.1109/tmi.2008.918330).

- 410 Ecabert, O., Peters, J., Walker, M. J., Ivanc, T., Lorenz, C., von Berg, J.,  
411 Lessick, J., Vembar, M., & Weese, J. (2011). Segmentation of the heart  
412 and great vessels in CT images using a model-based adaptation framework.  
413 *Medical Image Analysis*, *15*, 863–876. doi:[10.1016/j.media.2011.06.004](https://doi.org/10.1016/j.media.2011.06.004).
- 414 Eleid, M. F., Sorajja, P., Michelena, H. I., Malouf, J. F., Scott, C. G., &  
415 Pellikka, P. A. (2013). Flow-gradient patterns in severe aortic stenosis  
416 with preserved ejection fraction. *Circulation*, *128*, 1781–1789. doi:[10.1161/  
417 circulationaha.113.003695](https://doi.org/10.1161/circulationaha.113.003695).
- 418 Eweborn, G. W., Schirmer, H., Heggelund, G., Lunde, P., & Rasmussen, K.  
419 (2012). The evolving epidemiology of valvular aortic stenosis. the tromsø  
420 study. *Heart*, *99*, 396–400. doi:[10.1136/heartjnl-2012-302265](https://doi.org/10.1136/heartjnl-2012-302265).
- 421 Garcia, J., Kadem, L., Larose, E., Clavel, M.-A., & Pibarot, P. (2011). Com-  
422 parison between cardiovascular magnetic resonance and transthoracic doppler  
423 echocardiography for the estimation of effective orifice area in aortic steno-  
424 sis. *Journal of Cardiovascular Magnetic Resonance*, *13*, 25. doi:[10.1186/  
425 1532-429x-13-25](https://doi.org/10.1186/1532-429x-13-25).
- 426 Grbic, S., Ionasec, R., Vitanovski, D., Voigt, I., Wang, Y., Georgescu, B.,  
427 Navab, N., & Comaniciu, D. (2012). Complete valvular heart appara-  
428 tus model from 4d cardiac CT. *Medical Image Analysis*, *16*, 1003–1014.  
429 doi:[10.1016/j.media.2012.02.003](https://doi.org/10.1016/j.media.2012.02.003).
- 430 Hughes, S. W., D’Arcy, T. J., Maxwell, D. J., Saunders, J. E., Ruff, C. F.,  
431 Chiu, W. S., & Sheppard, R. J. (1996). Application of a new discreet form of  
432 gauss’ theorem for measuring volume. *Physics in medicine and biology*, *41*,  
433 1809–1821.
- 434 Ionasec, R. I., Voigt, I., Georgescu, B., Wang, Y., Houle, H., Vega-Higuera, F.,  
435 Navab, N., & Comaniciu, D. (2010). Patient-specific modeling and quantifi-  
436 cation of the aortic and mitral valves from 4-d cardiac CT and TEE. *IEEE  
437 Transactions on Medical Imaging*, *29*, 1636–1651. doi:[10.1109/tmi.2010.  
438 2048756](https://doi.org/10.1109/tmi.2010.2048756).

- 439 Lui, E. Y., Steinman, A. H., Cobbold, R. S., & Johnston, K. W. (2005). Human  
440 factors as a source of error in peak doppler velocity measurement. *Journal of*  
441 *Vascular Surgery*, *42*, 972.e1–972.e10. doi:[10.1016/j.jvs.2005.07.014](https://doi.org/10.1016/j.jvs.2005.07.014).
- 442 Menter, F. R. (1994). Two-equation eddy-viscosity turbulence models for engi-  
443 neering applications. *AIAA Journal*, *32*, 1598–1605. doi:[10.2514/3.12149](https://doi.org/10.2514/3.12149).
- 444 Nicoud, F., & Ducros, F. (1999). Subgrid-scale stress modelling based on the  
445 square of the velocity gradient tensor. *Flow, Turbulence and Combustion*, *62*,  
446 183–200. doi:[10.1023/a:1009995426001](https://doi.org/10.1023/a:1009995426001).
- 447 Nishimura, R. A., Otto, C. M., Bonow, R. O., Carabello, B. A., Erwin, J. P.,  
448 Guyton, R. A., O’Gara, P. T., Ruiz, C. E., Skubas, N. J., Sorajja, P., Sundt,  
449 T. M., & Thomas, J. D. (2014). 2014 AHA/ACC guideline for the manage-  
450 ment of patients with valvular heart disease. *Journal of the American College*  
451 *of Cardiology*, *63*, e57–e185. doi:[10.1016/j.jacc.2014.02.536](https://doi.org/10.1016/j.jacc.2014.02.536).
- 452 Nkomo, V. T., Gardin, J. M., Skelton, T. N., Gottdiener, J. S., Scott,  
453 C. G., & Enriquez-Sarano, M. (2006). Burden of valvular heart diseases:  
454 a population-based study. *Lancet (London, England)*, *368*, 1005–1011.  
455 doi:[10.1016/S0140-6736\(06\)69208-8](https://doi.org/10.1016/S0140-6736(06)69208-8).
- 456 Traeger, B., Srivatsa, S. S., Beussman, K. M., Wang, Y., Suzen, Y. B., Rybicki,  
457 F. J., Mazur, W., & Miszalski-Jamka, T. (2015). Methodological inaccuracies  
458 in clinical aortic valve severity assessment: insights from computational fluid  
459 dynamic modeling of CT-derived aortic valve anatomy. *Theoretical and Com-*  
460 *putational Fluid Dynamics*, *30*, 107–128. doi:[10.1007/s00162-015-0370-9](https://doi.org/10.1007/s00162-015-0370-9).
- 461 Vasudevan, V., Low, A. J. J., Annamalai, S. P., Sampath, S., Chin, C.-L.,  
462 Ali, A. A. B., & Yap, C. H. (2019). Role of diastolic vortices in flow and  
463 energy dynamics during systolic ejection. *Journal of Biomechanics*, *90*, 50–  
464 57. doi:[10.1016/j.jbiomech.2019.04.026](https://doi.org/10.1016/j.jbiomech.2019.04.026).
- 465 Vogelgesang, A., Hasenfuss, G., & Jacobshagen, C. (2017). Low-flow/low-

- 466 gradient aortic stenosis-still a diagnostic and therapeutic challenge. *Clinical*  
467 *Cardiology*, *40*, 654–659. doi:[10.1002/clc.22728](https://doi.org/10.1002/clc.22728).
- 468 Weese, J., Lungu, A., Peters, J., Weber, F. M., Waechter-Stehle, I., & Hose,  
469 D. R. (2017). CFD- and bernoulli-based pressure drop estimates: A compar-  
470 ison using patient anatomies from heart and aortic valve segmentation of CT  
471 images. *Medical Physics*, *44*, 2281–2292. doi:[10.1002/mp.12203](https://doi.org/10.1002/mp.12203).
- 472 Yang, C.-S., Marshall, E. S., Fanari, Z., Kostal, M. J., West, J. T., Kolm,  
473 P., Weintraub, W. S., & Doorey, A. J. (2015). Discrepancies between direct  
474 catheter and echocardiography-based values in aortic stenosis. *Catheterization*  
475 *and Cardiovascular Interventions*, *87*, 488–497. doi:[10.1002/ccd.26033](https://doi.org/10.1002/ccd.26033).
- 476 Zoghbi, W. A., Adams, D., Bonow, R. O., Enriquez-Sarano, M., Foster, E.,  
477 Grayburn, P. A., Hahn, R. T., Han, Y., Hung, J., Lang, R. M., Little, S. H.,  
478 Shah, D. J., Shernan, S., Thavendiranathan, P., Thomas, J. D., & Weissman,  
479 N. J. (2017). Recommendations for noninvasive evaluation of native valvular  
480 regurgitation. *Journal of the American Society of Echocardiography*, *30*, 303–  
481 371. doi:[10.1016/j.echo.2017.01.007](https://doi.org/10.1016/j.echo.2017.01.007).

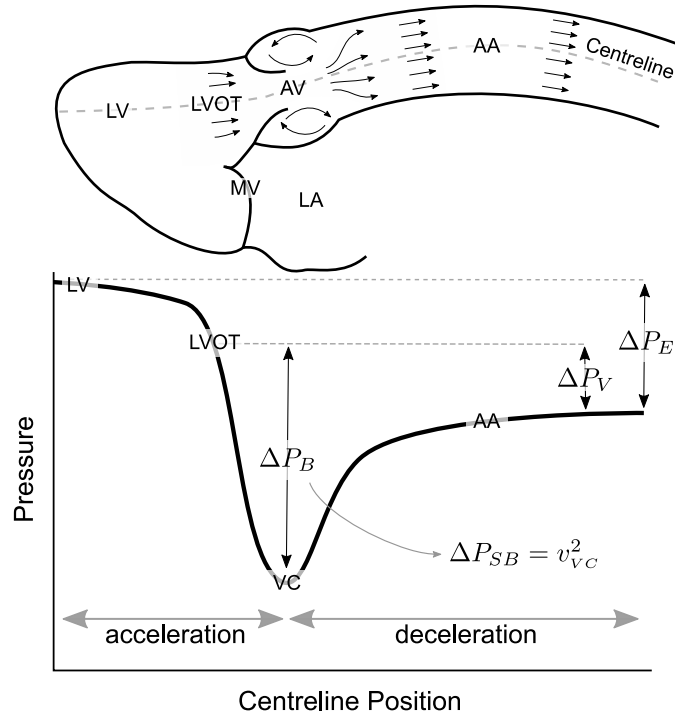


Figure 1: Top: schematic of the Left Ventricle (LV), Left Ventricular Outflow Tract (LVOT), Aortic Valve (AV), Vena Contracta (VC) and Ascending Aorta (AA). Bottom: typical pressure along the centreline.  $\Delta P_V$ : net pressure drop across the AV.  $\Delta P_E$ : effective pressure drop between the LV and AA.  $\Delta P_B$ : Bernoulli estimate, i.e. the maximum pressure drop across the valve,  $\Delta P_{SB}$ : simplified Bernoulli estimate from VC velocity. Mitral Valve (MV) and Left Atrium (LA) are added for anatomical reference.

Table 1: Pressure drop results over multiple cardiac cycles for case 11

	Cycle 1	Cycle 2	Cycle 3	Cycle 4	Cycle 5
$P_{LV}$ [mmHg]	6.86	6.90	6.89	6.88	6.94
$P_{LVOT}$ [mmHg]	3.42	3.44	3.43	3.43	3.49
$I_{VR}$ [-]	0.499	0.499	0.498	0.498	0.503

Note: simulations performed with a time-step of  $1 \cdot 10^{-3}$ s to limit simulation times.

[8] added this table to justify simulating a single cycle

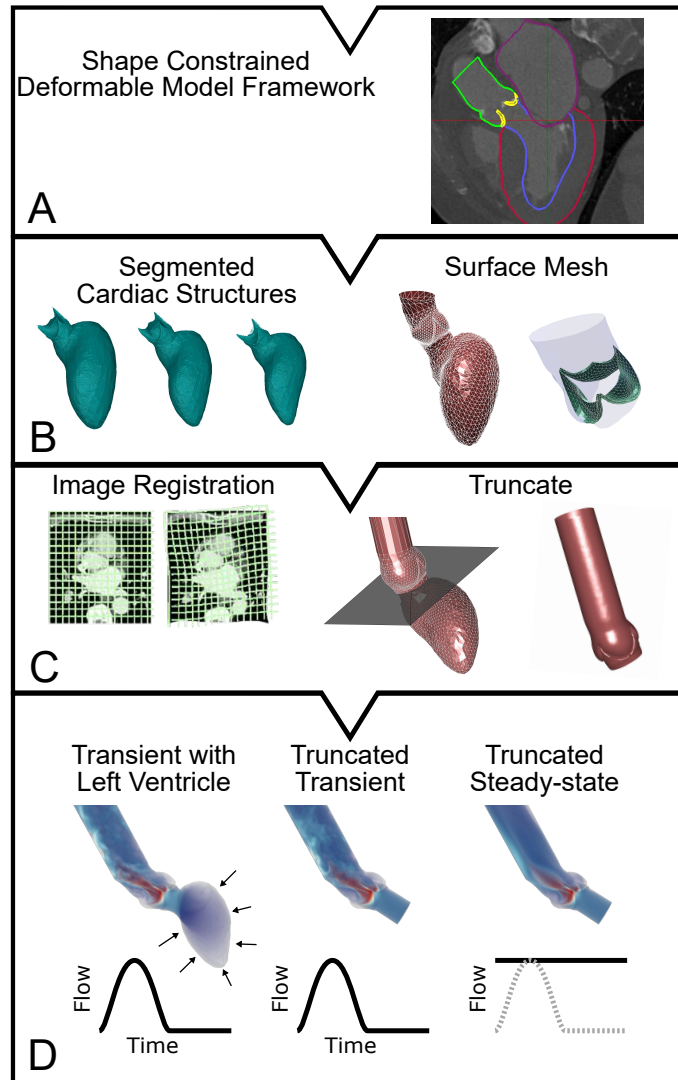


Figure 2: Illustration of the workflow from A) the Shape Constrained Deformable Model framework (Ecabert et al., 2011; Weese et al., 2017); B) Segmented aortic valve and left ventricle and corresponding structured surface mesh; C) image registration and mesh truncation; D) 4D CFD Model of the AV and contracting ventricle, 3D truncated transient model, and 3D truncated steady-state model.

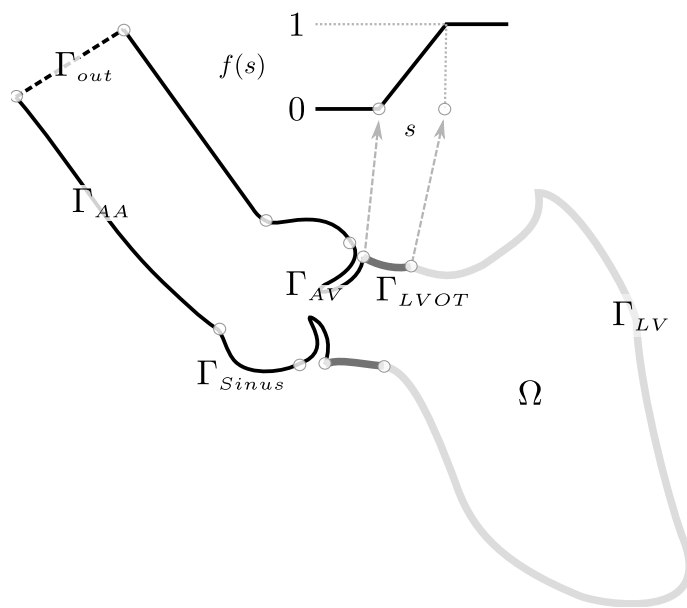


Figure 3: Boundary and domain definitions. Boundaries  $\Gamma_{LV}$  (light gray line) and  $\Gamma_{LVOT}$  (dark gray line) are deforming.  $\Gamma_{AV}$ ,  $\Gamma_{Sinus}$ ,  $\Gamma_{AA}$  (black lines) and  $\Gamma_{out}$  (dashed line) are static boundaries, i.e.  $\vec{v}_g$  is zero. Boundary motion is scaled to zero in the LVOT by a ramp function  $f(s)$ , with  $s$  the position in the LVOT



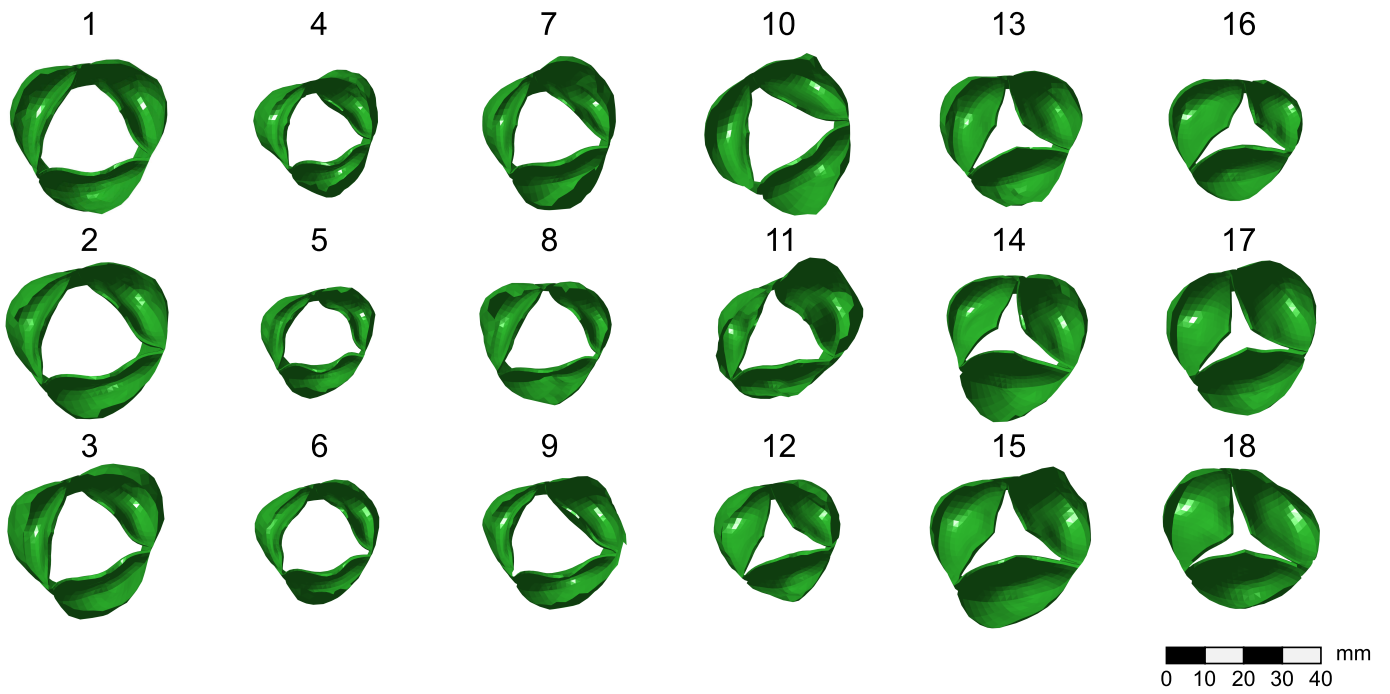


Figure 4: Axial view of the segmented AV for all cases. Cases 1-9 have a  $I_{VR} < 0.25$ , cases 10 and 11  $0.25 < I_{VR} < 0.75$ , and cases 12-18 a  $I_{VR} > 0.75$ . Case numbering corresponds to Table 2.

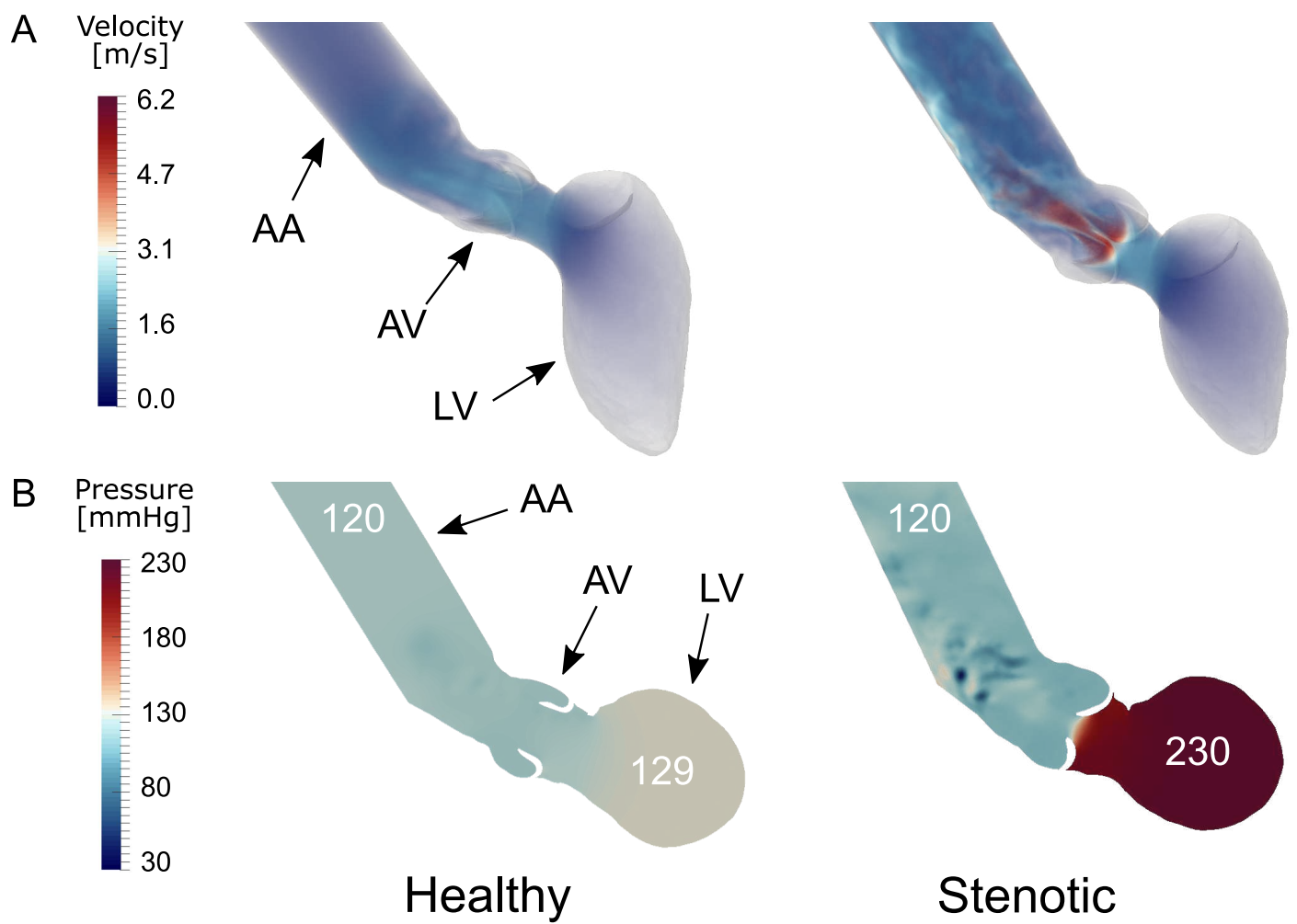


Figure 5: Volume renders of velocity (A) and contour plots of pressure (B) at peak systole for a healthy valve (left - case 8) and a stenotic valve (right - case 17).

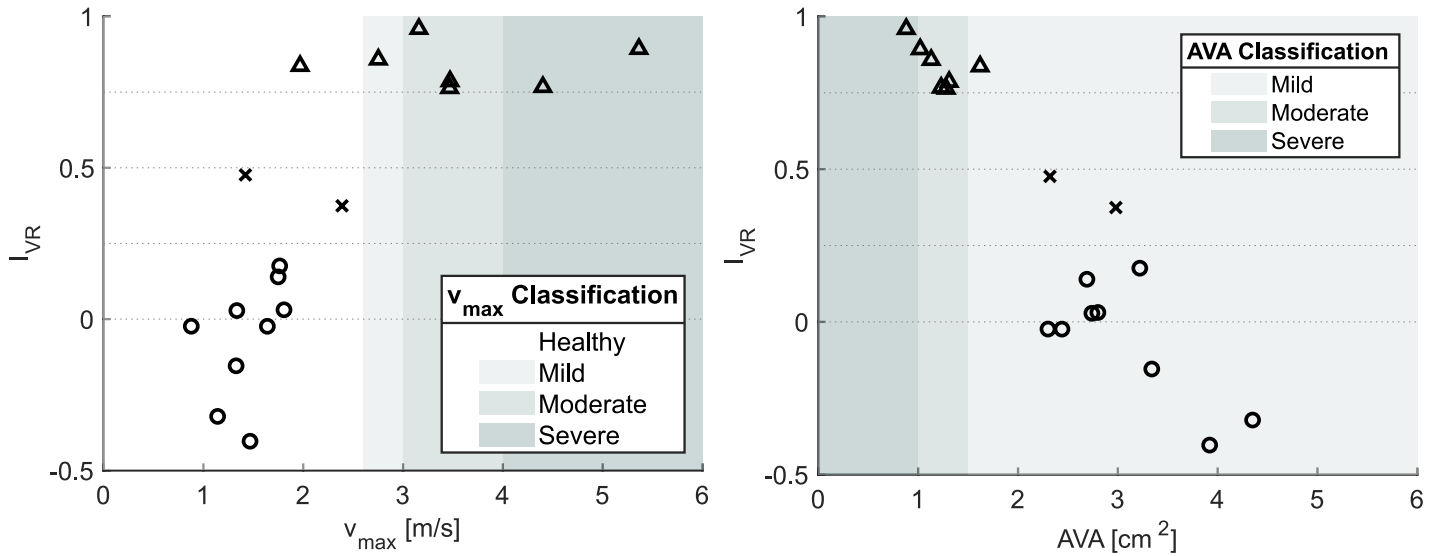


Figure 6: Left: CFD derived  $v_{max}$  vs. valve resistance index. Severity classifications are based on guidelines (Nishimura et al., 2014). Healthy:  $v_{max} < 2.6$  m/s. Mild:  $2.6$  m/s  $< v_{max} < 2.9$  m/s, moderate:  $3.0$  m/s  $< v_{max} < 4.0$  m/s, severe:  $v_{max} > 4.0$  m/s. Right: Geometric AVA vs. valve resistance index. Healthy/Mild: AVA  $> 1.5$   $cm^2$ , moderate:  $1.0$   $cm^2 < AVA < 1.5$   $cm^2$ , severe AVA  $< 1.0$   $cm^2$ . Furthermore, cases are separated in groups,  $I_{VR} < 0.25$  ( $\circ$ ),  $0.25 < I_{VR} < 0.75$  ( $\times$ ) and  $I_{VR} > 0.75$  ( $\triangle$ ). Note that the reported AVA is the geometric projected AVA, and not the effective orifice area (by echocardiography) as reported in the guidelines (Nishimura et al., 2014).

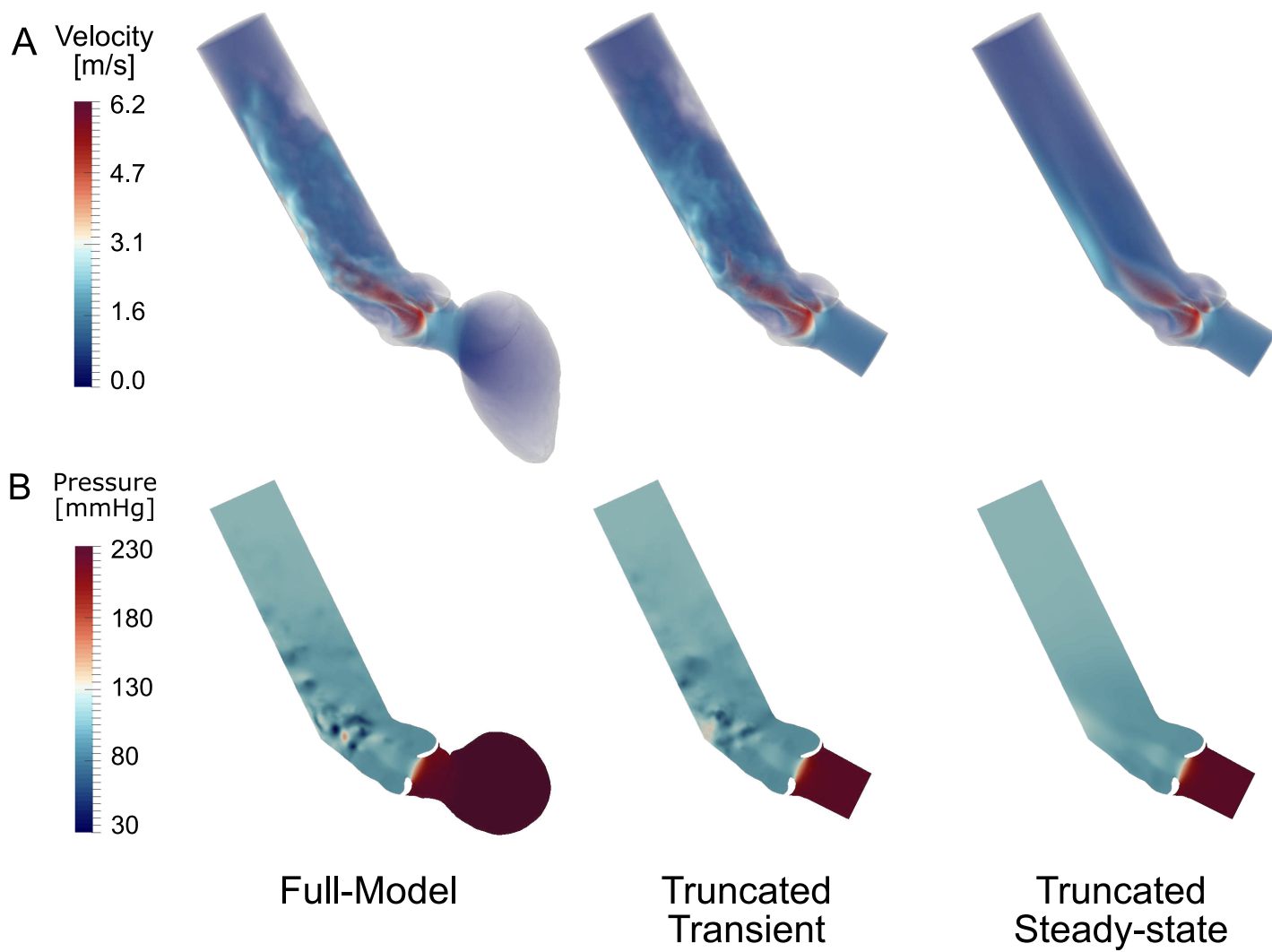


Figure 7: Volume render of velocity magnitude (A) and pressure contours (B) for each of the CFD models.

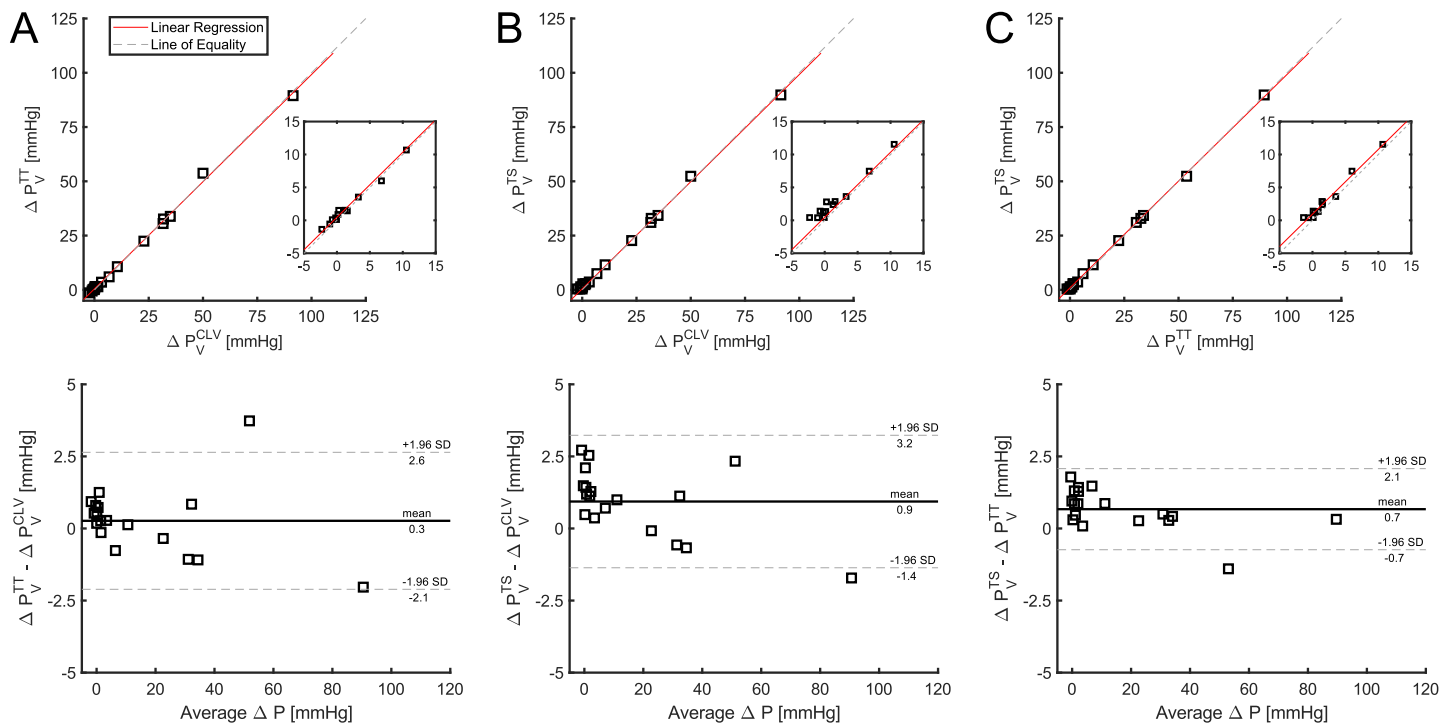


Figure 8: Comparison between CFD models and their respective  $\Delta P_V$ . Top row: scatter plot with linear regression results and line of equality. Bottom row: Bland-Altman of the difference. A) Transient truncated model vs. full model ( $R^2 = 0.998$ ); B) Truncated steady-state vs. full model ( $R^2 = 0.998$ ); C) Truncated steady-State vs. truncated transient model ( $R^2 = 0.999$ ).

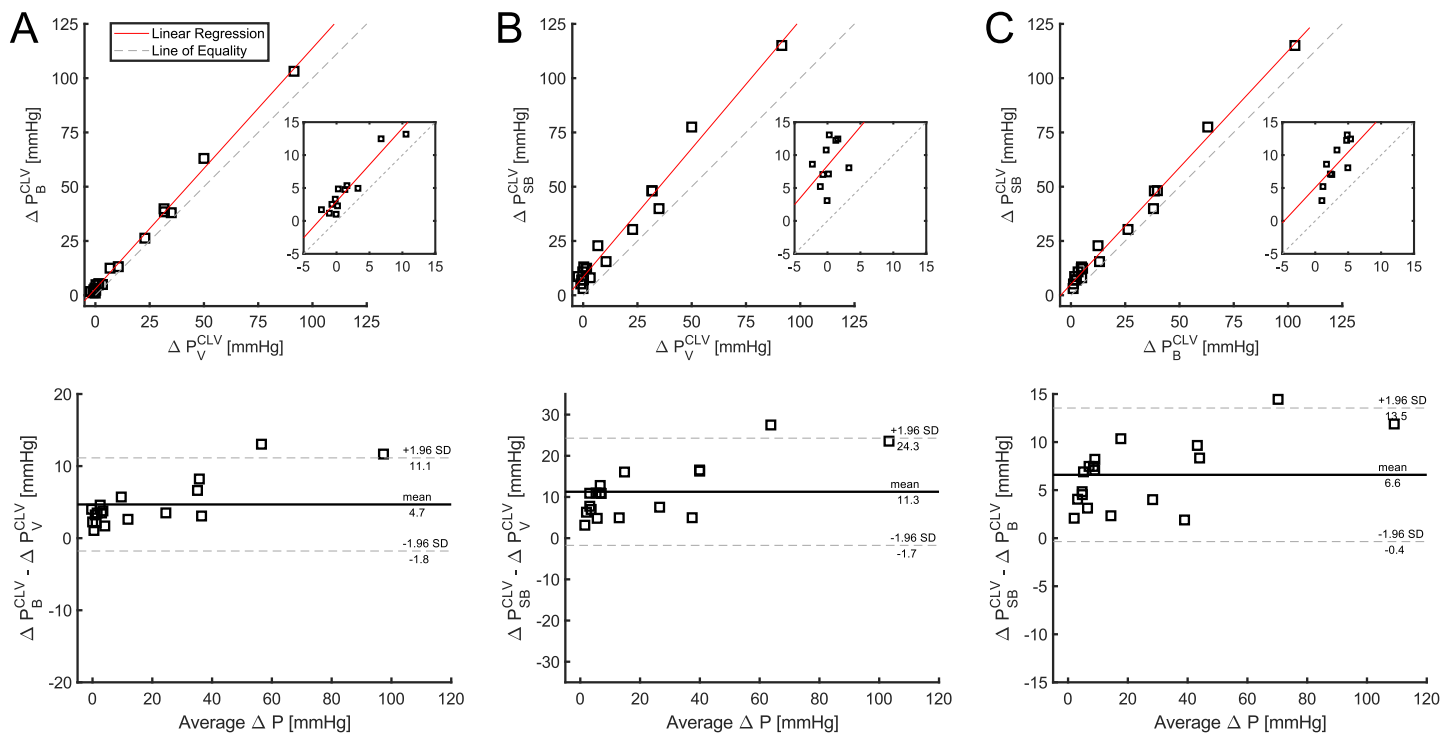


Figure 9: Comparison between the Bernoulli estimates and pressure drops computed with the full CFD model. A) Bernoulli estimate vs. full model ( $R^2 = 0.995$ ); B) Simplified Bernoulli ( $4v^2$ ) estimate vs. full model ( $R^2 = 0.973$ ); C) Simplified Bernoulli estimate vs. Bernoulli estimate ( $R^2 = 0.991$ ).

Table 2: Pressure drop estimates for each case and all models, ordered by valve resistance index

Case	HR bpm	$A_{LVOT}$ cm <sup>2</sup>	$A_{AV}$ cm <sup>2</sup>	$A_{AA}$ cm <sup>2</sup>	$Q_{max}$ ml/s	$v_{max}$ m/s	$\Delta P_E^{CLV}$ mmHg	$\Delta P_V^{CLV}$ mmHg	$\Delta P_V^{TT}$ mmHg	$\Delta P_V^{TS}$ mmHg	$\Delta P_B^{CLV}$ mmHg	$\Delta P_{SB}^{CLV}$ mmHg	$\nabla P_{LVOT}^{CLV}$ mmHg/mm	$I_{VR}^\dagger$ -2mm	$I_{VR}$ 0	$I_{VR}^\ddagger$ +2mm
1	73	4.8	3.9	10.1	489	1.47	5.7	-2.3	-1.4	0.4	1.7	8.6	-0.20	-0.33	-0.40	-0.47
2	56	5.5	4.3	14.7	433	1.14	3.4	-1.1	-0.6	0.4	1.2	5.2	-0.11	-0.25	-0.32	-0.39
3	66	4.6	3.3	9.5	397	1.33	4.6	-0.7	0.1	1.4	2.5	7.1	-0.15	-0.09	-0.15	-0.22
4	58	3.4	2.4	7.2	330	1.64	8.4	-0.2	0.4	1.2	3.3	10.8	-0.28	0.04	-0.02	-0.09
5	87	3.1	2.3	7.4	178	0.88	2.5	-0.1	0.1	0.4	1.0	3.1	-0.07	0.03	-0.02	-0.08
6	63	4.3	2.7	6.7	321	1.33	5.4	0.2	0.9	1.3	2.3	7.1	-0.18	0.09	0.03	-0.04
7	66	4.1	2.8	7.8	451	1.81	8.8	0.3	1.5	2.8	4.9	13.1	-0.25	0.09	0.03	-0.03
8	61	4.3	2.7	9.5	415	1.75	9.1	1.3	1.5	2.4	4.8	12.2	-0.32	0.21	0.14	0.07
9	66	4.5	3.2	10.2	488	1.76	9.0	1.6	1.4	2.9	5.4	12.4	-0.29	0.24	0.18	0.11
10	63	5.1	3.0	11.1	635	2.39	18.0	6.8	6.0	7.5	12.5	22.8	-0.70	0.45	0.37	0.30
11	67	4.5	2.3	12.1	296	1.42	6.8	3.3	3.5	3.6	5.0	8.1	-0.19	0.53	0.48	0.42
12	66	3.9	1.3	8.5	416	3.47	41.7	31.8	32.6	32.9	38.4	48.1	-0.63	0.79	0.76	0.73
13	74	3.8	1.2	9.3	510	4.40	65.2	50.0	53.7	52.3	63.0	77.5	-0.46	0.78	0.77	0.75
14	80	3.6	1.3	9.5	417	3.47	40.2	31.6	30.6	31.1	39.8	48.2	-0.40	0.81	0.79	0.77
15	82	5.8	1.6	11.9	302	1.97	12.6	10.6	10.7	11.5	13.2	15.5	-0.26	0.88	0.84	0.79
16	98	4.0	1.1	8.3	286	2.75	26.6	22.8	22.4	22.7	26.3	30.3	-0.26	0.88	0.86	0.84
17	57	4.7	1.0	10.9	511	5.36	102.5	91.5	89.5	89.8	103.2	115.1	-0.77	0.91	0.89	0.88
18	74	5.6	0.9	8.1	251	3.16	36.4	34.9	33.9	34.3	38.0	39.9	-0.19	0.97	0.96	0.95

<sup>†</sup> Valve resistance index when  $P_{LVOT}$  is taken 2 mm upstream truncation plane

<sup>‡</sup> Valve resistance index when  $P_{LVOT}$  is taken 2 mm downstream truncation plane

[9] added range in index and added LVOT and AA areas (R.1.7. & R 2.2.)